

Article

Nanoporous Ag-Decorated $\text{Ag}_7\text{O}_8\text{NO}_3$ Micro-Pyramids for Sensitive Surface-Enhanced Raman Scattering Detection

Linfan Guo ¹, Haibin Tang ², Xiujuan Wang ³, Yupeng Yuan ¹ and Chuhong Zhu ^{1,*}

¹ School of Chemistry and Chemical Engineering, School of Materials Science and Engineering, Anhui University, Hefei 230601, China

² Key Laboratory of Materials Physics, Anhui Key Laboratory of Nanomaterials and Nanotechnology, Institute of Solid State Physics, HFIPS, Chinese Academy of Sciences, Hefei 230031, China

³ School of Microelectronics, Hefei University of Technology, Hefei 230009, China

* Correspondence: chzhu@ahu.edu.cn or chzhu@issp.ac.cn

Abstract: Porous noble metal nanomaterials can be employed to construct sensitive surface-enhanced Raman scattering (SERS) substrates, because the plasmonic nanopores and nanogaps of the porous materials can provide a larger number of hotspots, and can also serve as containers of analyte molecules. However, the fabrication processes of nanoporous noble metal are generally complicated. Here, a facile method is presented to prepare nanoporous Ag nanoparticles-decorated $\text{Ag}_7\text{O}_8\text{NO}_3$ micro-pyramids, which are fabricated through the chemical reduction of the electrodeposited $\text{Ag}_7\text{O}_8\text{NO}_3$ micro-pyramids using NaBH_4 . The $\text{Ag}_7\text{O}_8\text{NO}_3$ micro-pyramids are fabricated by electrodeposition by using a simple aqueous solution of AgNO_3 as electrolyte. Then, porous Ag-decorated $\text{Ag}_7\text{O}_8\text{NO}_3$ micro-pyramids are achieved by the chemical reduction of the surface of the electrodeposited $\text{Ag}_7\text{O}_8\text{NO}_3$ micro-pyramids with NaBH_4 . The high-density nanopores and nanogaps of the fabricated nanoporous Ag can provide plenty of hot spots for Raman enhancement. Additionally, the nanopores have an effective capacity to trap and enrich analytes. Using rhodamine 6G (R6G) as a probe molecule, the SERS performance of the fabricated SERS substrate has been investigated. It is found that a limit of detection (LOD) $\sim 1.0 \times 10^{-15}$ M can be achieved for R6G. Then, the SERS substrates are employed to detect dye molecule (crystal violet) and pesticide (thiram), and their LODs are calculated down to 9.6×10^{-13} M and 1.3×10^{-15} M, respectively. The enhancement factor of the fabricated SERS substrate is estimated to be as high as 5.6×10^8 . Therefore, the nanoporous Ag-decorated $\text{Ag}_7\text{O}_8\text{NO}_3$ micro-pyramids have shown promising application in the sensitive SERS detection of organic molecules.

Keywords: surface-enhanced Raman scattering; detection; porous silver; pesticide; chemical reduction



Citation: Guo, L.; Tang, H.; Wang, X.; Yuan, Y.; Zhu, C. Nanoporous Ag-Decorated $\text{Ag}_7\text{O}_8\text{NO}_3$ Micro-Pyramids for Sensitive Surface-Enhanced Raman Scattering Detection. *Chemosensors* **2022**, *10*, 539. <https://doi.org/10.3390/chemosensors10120539>

Academic Editor: Brian Cullum

Received: 25 October 2022

Accepted: 14 December 2022

Published: 16 December 2022

Publisher's Note: MDPI stays neutral with regard to jurisdictional claims in published maps and institutional affiliations.



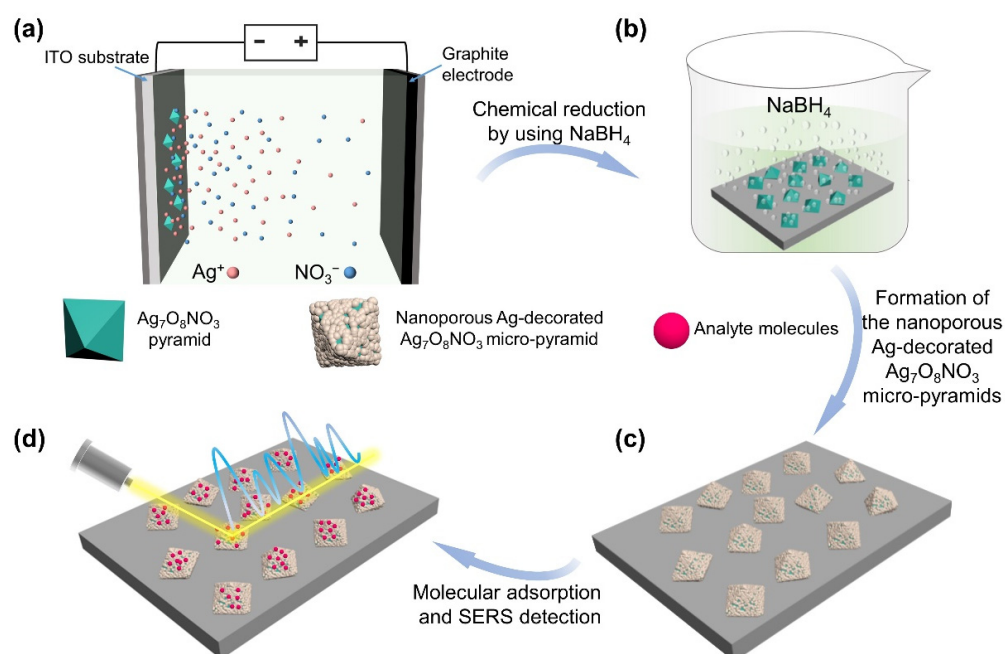
Copyright: © 2022 by the authors. Licensee MDPI, Basel, Switzerland. This article is an open access article distributed under the terms and conditions of the Creative Commons Attribution (CC BY) license (<https://creativecommons.org/licenses/by/4.0/>).

1. Introduction

Surface-enhanced Raman scattering (SERS) spectra can provide fingerprint information of molecular vibration with high sensitivity. Therefore, SERS can serve as an effective and convenient analytical tool, and has been utilized substantially in the rapid, sensitive, and nondestructive detection of chemical and biological agents [1–8]. A major driving force for achieving sensitive response to a substance's adsorption on a metal surface is localized surface plasmon resonance (LSPR). In particular, the collective plasmon resonance arising from the LSPR interaction of Ag and Au [9,10] is utilized by SERS. However, LSPR energies are dependent on the local dielectric environment, the size, shape, and composition of these metal nanostructures [11–14]. The methods for creating noble metal nanoparticles with sharp tips [7,14–16] or nano-gaps [17,18], as well as nanostars [19,20], nanoflowers [21,22], and porous nanoparticles [23–25], have been the subject of studies in recent years. For example, highly ordered arrays of solid gold and silver nanopyramids have been developed for reproducible and sensitive SERS detection [26–29]. Porous nanostructures have garnered a lot of attention as compared to other structures (e.g., the above-mentioned

arrays of solid gold and silver nanopyramids) because of their enormous relative surface area, high internal “hot spot” density, and optical properties linked to porosity [30–32]. In addition to having a high surface area, high gas permeability, and low density in a variety of porous materials, porous noble metal materials also possess surface plasmon resonance properties that have numerous uses in the optical field [32–35]. The fascinating networks of interconnected structures that make up the nanoporous metal structures have a morphology with tunable open pores and ligament sizes ranging from nanometers to micrometers, producing a significant amount of specific surface area [36,37]. Porous metal nanomaterials have so far been prepared using a variety of physical and chemical techniques, such as the template method [38–41], galvanic replacement [42–44], and dealloying method [45–47]. These methods make the preparation process extra intricate and expensive. Therefore, there is still a critical need to develop a facile and inexpensive approach for fabrication of nanoporous plasmonic structures with the capability to tailor the structural parameters for optimized performance.

Here, we present a rapid and cost-effective method to fabricate nanoporous Ag-decorated $\text{Ag}_7\text{O}_8\text{NO}_3$ micro-pyramids. By chemically reducing the $\text{Ag}_7\text{O}_8\text{NO}_3$ micro-pyramids, which had been prepared in advance by electrodeposition, nanoporous Ag-decorated $\text{Ag}_7\text{O}_8\text{NO}_3$ micro-pyramids with dense nanopores have been fabricated without using any organic chemicals or etching agents. As shown in Scheme 1a, the $\text{Ag}_7\text{O}_8\text{NO}_3$ micro-pyramids are firstly formed by electrodeposition. Then, the as-prepared $\text{Ag}_7\text{O}_8\text{NO}_3$ micro-pyramids are immersed in an aqueous solution of NaBH_4 (Scheme 1b). Using NaBH_4 as a reducing agent, nanoporous Ag-decorated $\text{Ag}_7\text{O}_8\text{NO}_3$ micro-pyramids are achieved by optimizing experimental conditions (Scheme 1c). Furthermore, we used the nanoporous Ag-decorated $\text{Ag}_7\text{O}_8\text{NO}_3$ micro-pyramids as SERS substrate to detect chemical molecules such as R6G, crystal violet (CV), and thiram. The nanoporous Ag-decorated $\text{Ag}_7\text{O}_8\text{NO}_3$ micro-pyramids showed excellent SERS performance with the capability to sensitively detect and identify organic pollutants. Therefore, the fabricated nanoporous Ag-decorated $\text{Ag}_7\text{O}_8\text{NO}_3$ micro-pyramids have promising applications in SERS-based detection.



Scheme 1. Schematic diagram of preparation process for the nanoporous Ag-decorated $\text{Ag}_7\text{O}_8\text{NO}_3$ micro-pyramids. (a) $\text{Ag}_7\text{O}_8\text{NO}_3$ micro-pyramids are fabricated using electrodeposition in a pure aqueous AgNO_3 solution with a two-electrode system. (b,c) $\text{Ag}_7\text{O}_8\text{NO}_3$ micro-pyramids are transformed into nanoporous Ag-decorated $\text{Ag}_7\text{O}_8\text{NO}_3$ micro-pyramids by NaBH_4 reduction. (d) Nanoporous Ag-decorated $\text{Ag}_7\text{O}_8\text{NO}_3$ micro-pyramids are used as SERS substrates to detect organic molecules.

2. Experimental

2.1. Materials

Silver nitrate (AgNO_3) was purchased from Sinopharm Chemical Reagent Co., Ltd. (Shanghai, China). Sodium borohydride (NaBH_4), Rhodamine 6G ($\text{C}_{28}\text{H}_{31}\text{ClN}_2\text{O}_3$), crystal violet ($\text{C}_{25}\text{H}_{30}\text{ClN}_3$), and thiram ($\text{C}_6\text{HN}_2\text{S}_4$) were purchased from Aladdin Bio-Chem Technology Co., Ltd. (Shanghai, China). Indium tin oxide (ITO) glasses were bought from Huanxiangcheng Technology Co., Ltd. (Shenzhen, China). Deionized water ($18.25 \text{ M}\Omega \text{ cm}^{-1}$) was obtained from a Millipore water purification.

2.2. Electrochemical Fabrication of $\text{Ag}_7\text{O}_8\text{NO}_3$ Micro-Pyramids

Electrochemical deposition was carried out using a two-electrode system, as shown schematically in Scheme 1a. A rectangular graphite sheet was used as an anode, an ITO glass ($2 \text{ cm} \times 0.5 \text{ cm}$) was used as a cathode, and an aqueous solution of AgNO_3 (0.01 M) was employed as the electrolyte. At room temperature, the potentiostatic mode was applied for the electrodeposition of $\text{Ag}_7\text{O}_8\text{NO}_3$ micro-pyramids. By regulating electrodeposition voltage from 1.5 V to 10 V or deposition duration from 1 s to 300 s, $\text{Ag}_7\text{O}_8\text{NO}_3$ materials with different micro-structures were achieved. Then the ITO glass coated with the as-prepared $\text{Ag}_7\text{O}_8\text{NO}_3$ micro-pyramids was taken out, rinsed with deionized water, and dried by flowing Ar gas.

2.3. Formation of Nanoporous Ag-Decorated $\text{Ag}_7\text{O}_8\text{NO}_3$ Micro-Pyramids

An ITO glass covered with $\text{Ag}_7\text{O}_8\text{NO}_3$ micro-pyramids was vertically immersed into an aqueous solution of NaBH_4 (10 mL) with different concentrations for 2 min to reduce silver ion on the surface of the $\text{Ag}_7\text{O}_8\text{NO}_3$ micro-pyramids into Ag atoms for formation of nanoporous Ag-decorated $\text{Ag}_7\text{O}_8\text{NO}_3$ micro-pyramids. After the reduction process, the ITO glass coated with the fabricated nanoporous Ag-decorated $\text{Ag}_7\text{O}_8\text{NO}_3$ micro-pyramids was taken out, rinsed with deionized water, and dried by flowing Ar gas.

2.4. Characterization and SERS Measurements

The resultant compact $\text{Ag}_7\text{O}_8\text{NO}_3$ micro-pyramids and nanoporous Ag-decorated $\text{Ag}_7\text{O}_8\text{NO}_3$ micro-pyramids were characterized by using X-ray diffraction (XRD, Rigaku SmartLab, Beijing Co, Beijing, China), X-ray photoelectron spectroscopy (XPS, Thermo ESCALAB 250Xi, Waltham, MA, USA) scanning electron microscope (SEM, Hitachi S-4800, Hitachi, Tokyo, Japan), and transmission electron microscope (TEM, JEM-2100F, JEOL, Tokyo, Japan). SERS measurement was conducted on a confocal microprobe Raman system (inVia, Renishaw, London, UK) with a 532 nm excitation laser. The laser power was $\sim 1 \text{ mW}$, and the integration duration was 10 s.

2.5. Preparation of SERS Sample

To ensure good adsorption of analyte molecule, nanoporous Ag-decorated $\text{Ag}_7\text{O}_8\text{NO}_3$ micro-pyramids on an ITO glass ($0.5 \text{ cm} \times 0.5 \text{ cm}$, Figure S1) were immersed in an aqueous solution (10 mL) of R6G, CV or an ethanol solution (10 mL) of thiram with different concentrations for 2 h, then taken out and dried with flowing Ar gas. During SERS measurement, 10 different points were randomly selected on each substrate to analyze the SERS-spectral reproducibility of the substrate.

3. Results and Discussion

3.1. Characteristics of $\text{Ag}_7\text{O}_8\text{NO}_3$ Micro-Pyramids

$\text{Ag}_7\text{O}_8\text{NO}_3$ micro-pyramids are firstly fabricated by electrodeposition in a simple aqueous electrolyte of AgNO_3 . All the diffraction peaks observed in the X-ray diffraction pattern (XRD) of the as-prepared sample (Figure S2) correspond to an $\text{Ag}_7\text{O}_8\text{NO}_3$ crystal (JCPDS: 06-0434); these diffraction peaks are assigned to the (2 2 2), (4 0 0), (4 4 0), and (6 2 2) planes, indicating that $\text{Ag}_7\text{O}_8\text{NO}_3$ micro-pyramids have been successfully prepared [48]. The EDX mapping was conducted to confirm Ag and O distributions of $\text{Ag}_7\text{O}_8\text{NO}_3$ micro-pyramids

(Figure S3), which are consistent with those reported previously [48]. The morphology of the fabricated $\text{Ag}_7\text{O}_8\text{NO}_3$ micro-pyramids could be regulated by tuning the deposition voltage and deposition duration [49–52]. Firstly, the morphological evolution of the pyramids was investigated by gradually increasing the deposition voltage from 1.5 to 10 V while the deposition time was kept unchanged (Figure S4). Sparsely distributed $\text{Ag}_7\text{O}_8\text{NO}_3$ micro-pyramids were preliminarily formed at 1.5 V with an average edge length of 650 nm (Figure S4a). With the increase of deposition voltage, the density of $\text{Ag}_7\text{O}_8\text{NO}_3$ micro-pyramids was increased accordingly (Figure S4b–d). Under a deposition voltage of 3 V, pyramids with an average edge of $\sim 1.5 \mu\text{m}$ were formed and uniformly distributed on an ITO glass (Figure S4b). Nevertheless, with further increase of deposition voltage from 3 V to 5 V or even 10 V, arrowhead-like particles with a smaller size were achieved (Figure S4c,d), due to the presence of the electrocarving process at high deposition voltages. The change in pyramid size can be explained by the fact that more $\text{Ag}_7\text{O}_8\text{NO}_3$ nuclei produced during the same deposition time at higher deposition voltages ($>5 \text{ V}$). High deposition voltages produce more $\text{Ag}_7\text{O}_8\text{NO}_3$ species than low deposition voltages, but because of the large number of nuclei, only a limited number of $\text{Ag}_7\text{O}_8\text{NO}_3$ species that can be consumed at once. As a result, smaller $\text{Ag}_7\text{O}_8\text{NO}_3$ pyramids are formed at high deposition voltages. This can be proved by the number density of $\text{Ag}_7\text{O}_8\text{NO}_3$ pyramid (Figure S4c,d), which increases quickly as the deposition voltage enhanced [48]. In this work, we focus on the pyramid-like structures, therefore the voltage used for deposition was set as 3 V in the following experiments.

Then, we further studied the growth process of the pyramids under different duration of electrodeposition by keeping the deposition voltage (3 V) unchanged (Figure S5). Quasi-pyramid-like nanoparticles with a rough surface were formed in a very short time (1 s) (Figure S5a). As the deposition duration increased, more regular pyramid structures with larger size were gradually formed (Figure S5b–d). Larger plasmonic particle has a larger surface area, which can provide more adsorption sites for analyte molecules [53,54]. Therefore, the $\text{Ag}_7\text{O}_8\text{NO}_3$ micro-pyramids with largest size were used to fabricate SERS-active structures since they can provide more hotspots in the excitation laser beam for SERS detection. Hence, the samples achieved under the voltage of 3 V and electrodeposition duration of 300 s were employed for SERS detection in the following experiments.

3.2. Fabrication of Nanoporous Ag-Decorated $\text{Ag}_7\text{O}_8\text{NO}_3$ Micro-Pyramids

Figure 1a shows the scanning electron microscope (SEM) image of the as-prepared $\text{Ag}_7\text{O}_8\text{NO}_3$ micro-pyramids. The $\text{Ag}_7\text{O}_8\text{NO}_3$ micro-pyramids have a smooth surface with an average edge length of $\sim 3.2 \mu\text{m}$. It can be found that the electrodeposited $\text{Ag}_7\text{O}_8\text{NO}_3$ micro-structure tends to form an octahedral shape. After fabrication of $\text{Ag}_7\text{O}_8\text{NO}_3$ micro-pyramids, we decorate SERS-active material on their surfaces by an in situ reduction method [21,55]. After being reduced by NaBH_4 , porous Ag was formed and uniformly modified on the surface of each $\text{Ag}_7\text{O}_8\text{NO}_3$ micro-pyramid (Figure 1b). The reduced Ag was uniformly assembled on the surface of $\text{Ag}_7\text{O}_8\text{NO}_3$ micro-pyramids and formed a nanoporous Ag shell coated on the micro-pyramids (Figure 1b). Transmission electron microscopy (TEM) observation indicates that the Ag nanostructures on the $\text{Ag}_7\text{O}_8\text{NO}_3$ micro-pyramids are well crystallized (Figure 1c). The spacing between adjacent lattice fringes was 0.237 nm for Ag (inset in Figure 1c), which agree well with the interplanar distance of the (1 1 1) plane of metallic Ag (JCPDS: 04-0783). The nanoporous Ag shell is composed of many cross-linked ellipsoidal and/or rod-shaped Ag nanostructures (Figure 1d,e). The EDX mapping was conducted to confirm the element distributions of nanoporous Ag-decorated $\text{Ag}_7\text{O}_8\text{NO}_3$ micro-pyramids (Figure S6), which is consistent with that reported previously [48]. Then, X-ray diffraction spectrum measurement was further performed to investigate the crystal structure of the nanoporous Ag-decorated $\text{Ag}_7\text{O}_8\text{NO}_3$ micro-pyramids (Figure 1f). The XRD pattern confirms that the sample are composed of two crystallized components: Ag and $\text{Ag}_7\text{O}_8\text{NO}_3$. The XRD spectrum display the peaks around 38.1° , 44.3° and 64.4° correspond to the diffractions from the (1 1 1),

(2 0 0) and (2 2 0) planes of the face-centered-cubic (fcc) phase, respectively (upper curve in Figure 1f), confirming that the resultant sample contains abundant Ag crystals. These results demonstrate that nanoporous Ag has been successfully decorated on the surfaces of $\text{Ag}_7\text{O}_8\text{NO}_3$ micro-pyramids by NaBH_4 reduction. Such nanoporous Ag-decorated $\text{Ag}_7\text{O}_8\text{NO}_3$ micro-pyramids can be employed as three-dimensional SERS substrates for sensitive detection [13,14].

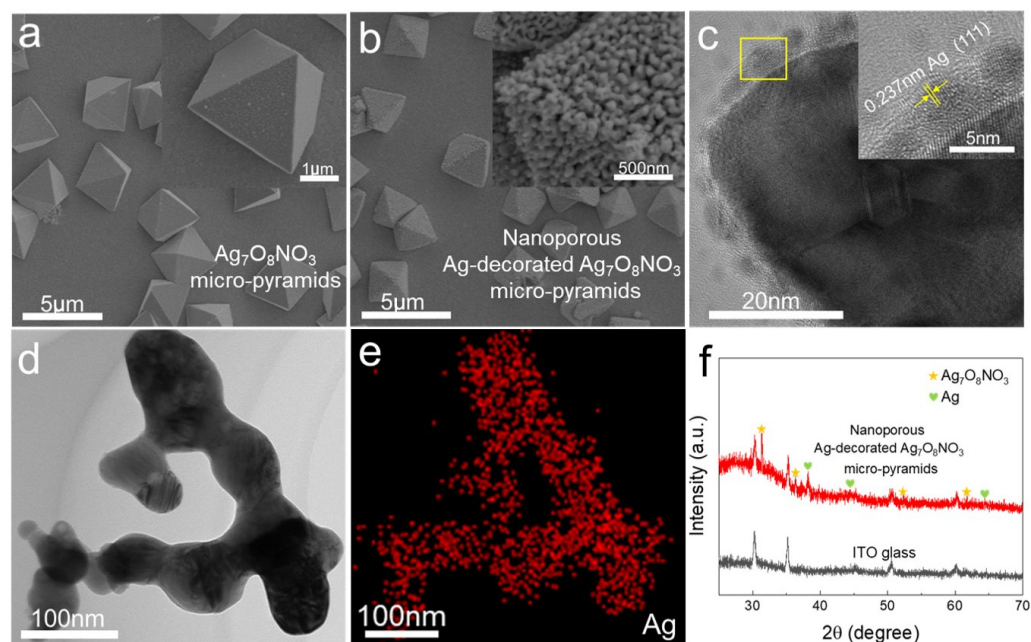


Figure 1. (a) SEM image of the $\text{Ag}_7\text{O}_8\text{NO}_3$ micro-pyramids fabricated by electrodeposition at 3 V for 300 s. The inset is a magnified image. (b) SEM image of the nanoporous Ag-decorated $\text{Ag}_7\text{O}_8\text{NO}_3$ micro-pyramids prepared by reducing the surface of $\text{Ag}_7\text{O}_8\text{NO}_3$ in a NaBH_4 solution. The inset is a magnified image. (c) TEM image of nanoporous Ag, and the inset is the corresponding high-resolution transmission electron microscopy (HRTEM) image marked in the yellow box in (c). (d) TEM image of Ag nanostructure peeled off from a nanoporous Ag-decorated $\text{Ag}_7\text{O}_8\text{NO}_3$ micro-pyramid through ultrasonic. (e) Corresponding elemental mapping of Ag collected from the area shown in (d). (f) XRD patterns of (upper curve) the prepared nanoporous Ag-decorated $\text{Ag}_7\text{O}_8\text{NO}_3$ micro-pyramids and (lower curve) an ITO glass.

During the process of decorating nanoporous Ag on the $\text{Ag}_7\text{O}_8\text{NO}_3$ micro-pyramids, the concentration of the reducing agent (i.e., NaBH_4) plays an important role on the morphology of the reduction-produced Ag nanostructures. When the concentration of NaBH_4 is very low, only a few Ag nanoparticles were anchored on the surface of the $\text{Ag}_7\text{O}_8\text{NO}_3$ micro-pyramids (Figure 2a) after the $\text{Ag}_7\text{O}_8\text{NO}_3$ micro-pyramids being immersed in an aqueous solution of NaBH_4 (1 mM) for 2 min. When the concentration of NaBH_4 increased to a moderate level (e.g., 5 mM), a larger amount of Ag plenty of nanopores were decorated on the surfaces of the $\text{Ag}_7\text{O}_8\text{NO}_3$ pyramids (Figure 2b). If the NaBH_4 concentration continued to increase to a much higher value (e.g., 10 mM or 25 mM), the Ag nano-ligaments constantly cumulated, and the number of pores in the Ag nanofilm decreased remarkably (Figure 2c,d). The disappearance of nanometer-sized ligaments and pores would decrease the number of hotspots, and thus lower the SERS activity of the fabricated hybrid micro/nanostructures. To optimize SERS performance, the R6G (10^{-6} M) was used as a probe molecule for Raman measurement. The SERS activity of the Ag-decorated $\text{Ag}_7\text{O}_8\text{NO}_3$ micro-pyramids achieved under different concentrations of NaBH_4 solution changed obviously (Figure S7a). In order to observe the variation trend of Raman intensity more intuitively, Raman intensities at 1648 cm^{-1} peak obtained by using different samples prepared under different concentrations of NaBH_4 are shown in Figure S7b. It can be found

that the optimized SERS performance was obtained at NaBH_4 concentration of 5 mM. The silver ligaments of the resultant nanoporous Ag are composed of numerous irregular cross-linked ellipsoidal and/or rod-shaped Ag nanostructures (Figure S8a), and the pores and ligaments sizes of the nanoporous Ag-decorated $\text{Ag}_7\text{O}_8\text{NO}_3$ micro-pyramids were around 41.6 nm and 48.8 nm (Figure S8b,c), respectively. The high-density nanopores (with an average diameter of ~ 40 nm) and nanogaps in the fabricated nanoporous Ag can provide plenty of hot spots for Raman enhancement. Additionally, the nanopores have an effective capacity to trap and enrich analyte molecules, resulting in further improvement of SERS sensitivity [56–58]. Therefore, the nanoporous Ag-decorated $\text{Ag}_7\text{O}_8\text{NO}_3$ micro-pyramids reduced using 5 mM NaBH_4 solution will be used as for sensitive SERS detection in the following tests.

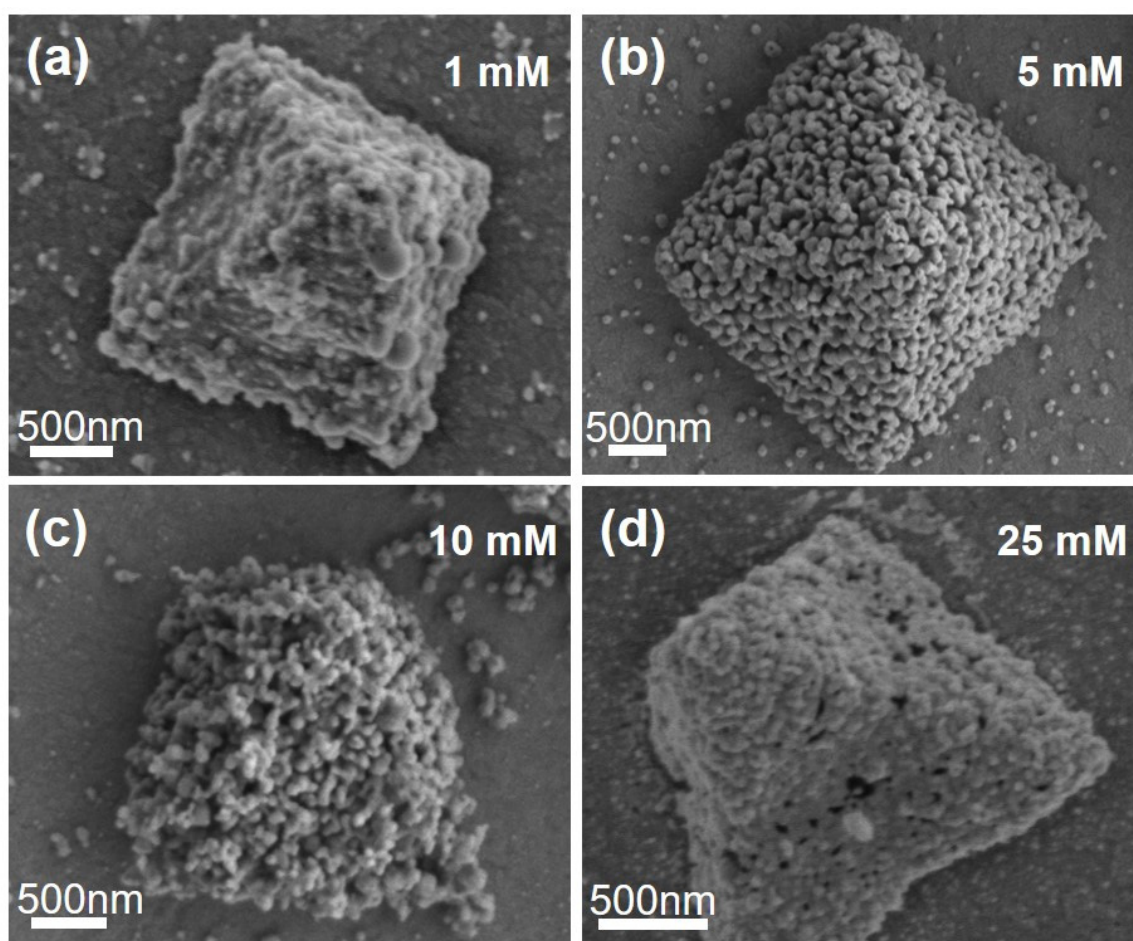


Figure 2. SEM images of the nanoporous Ag-decorated $\text{Ag}_7\text{O}_8\text{NO}_3$ micro-pyramids fabricated by using NaBH_4 solution with different concentrations: (a) 1 mM; (b) 5 mM; (c) 10 mM; and (d) 25 mM.

3.3. SERS Performance

Sensitivity is an important criterion for the performance of SERS substrates. For exploring the SERS activity of the nanoporous Ag-decorated $\text{Ag}_7\text{O}_8\text{NO}_3$ micro-pyramids, a frequently used organic substance, R6G, was used as a probe molecule. In order to understand the origin of Raman signal enhancement, the SERS activities of $\text{Ag}_7\text{O}_8\text{NO}_3$ micro-pyramids before and after being decorated with nanoporous Ag were measured. It is found that the $\text{Ag}_7\text{O}_8\text{NO}_3$ micro-pyramids do not possess SERS activity (Curve II in Figure S9) and the nanoporous Ag decorated on the $\text{Ag}_7\text{O}_8\text{NO}_3$ microstructures has remarkable SERS activity (Curve I in Figure S9). Therefore, the SERS activity is contributed by the nanoporous Ag. The most pronounced bands of R6G molecules appear at 612 (C-C-C ring in-plane vibration), 775 (C-C-C-ring out-of-plane bending), 1362 (aromatic C-C stretching),

1508 (aromatic C-C stretching), and 1648 (aromatic C-C stretching) cm^{-1} [59]. Additionally, a linear relationship between the logarithmic concentrations of R6G and the fingerprint peaks (1648 cm^{-1}) was discovered (Figure 3b) as shown below:

$$\log I = 5.49 + 0.27 \log C \quad (1)$$

where I is the peak intensity of the SERS spectra of R6G, and C is the concentration of R6G. The linear fitting result shows that the R^2 value of R6G is 0.983, which proves that the nanoporous Ag-decorated $\text{Ag}_7\text{O}_8\text{NO}_3$ micro-pyramids have the ability of quantitative detection of R6G. According to the Formula (1), the limit of detection (LOD) of R6G could be calculated. The SERS signal intensity at the LOD is equivalent to three times of the standard deviation of Raman signal intensity from the blank sample [60–64]. The LOD of R6G was calculated to be 10^{-15} M, demonstrating that the fabricated nanoporous Ag-decorated $\text{Ag}_7\text{O}_8\text{NO}_3$ micro-pyramids substrate has excellent sensitivity for R6G. Compared with the LODs of R6G achieved by using the other SERS substrates reported in the previous literatures, our nanoporous Ag-decorated $\text{Ag}_7\text{O}_8\text{NO}_3$ micro-pyramids have a comparable or superior LOD (Supplementary Table S1 [65–72]).

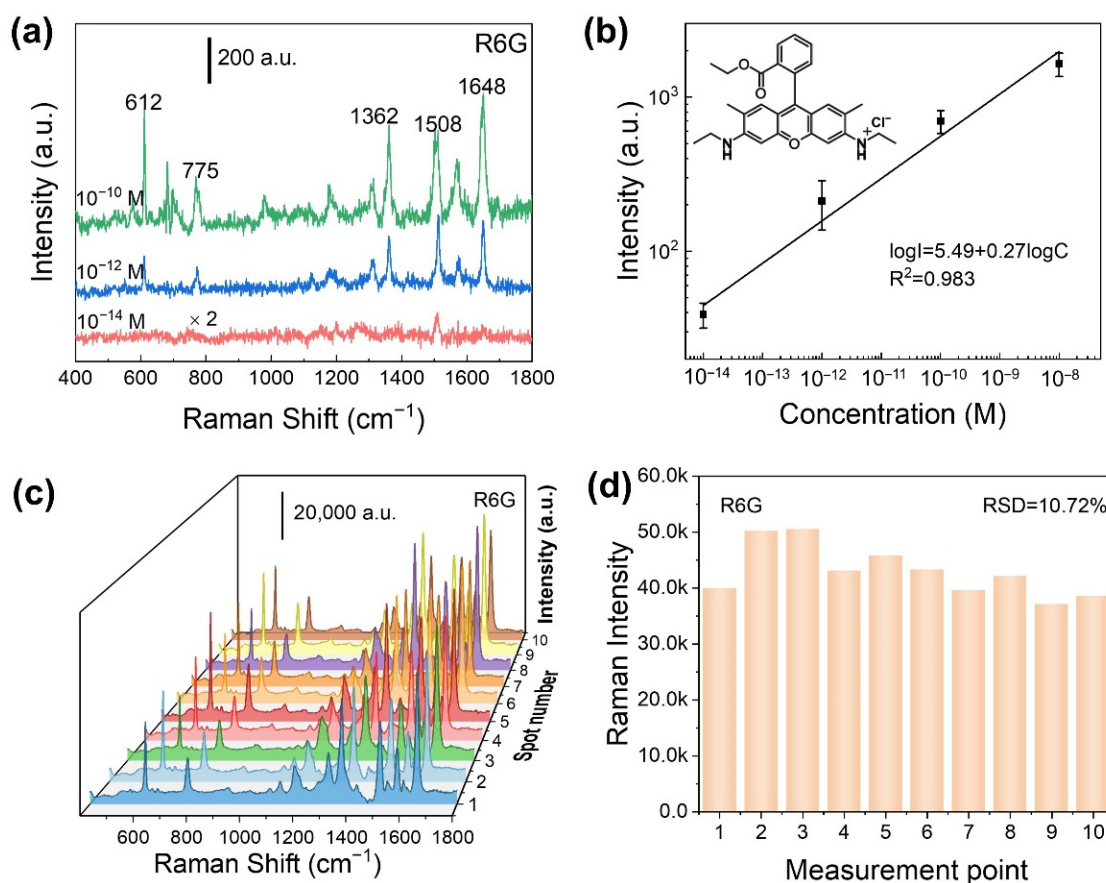


Figure 3. (a) SERS spectra of 10^{-10} , 10^{-12} and 10^{-14} M R6G collected from nanoporous Ag-decorated $\text{Ag}_7\text{O}_8\text{NO}_3$ micro-pyramids. (b) Linear relationship between the logarithmic intensities of 1648 cm^{-1} peak and the concentrations of R6G. (c) SERS spectra of R6G (10^{-6} M) at 10 randomly selected sites on the SERS substrate made of nanoporous Ag-decorated $\text{Ag}_7\text{O}_8\text{NO}_3$ micro-pyramids. (d) The 1648 cm^{-1} band intensities of R6G (10^{-6} M) recorded from 10 randomly selected sites.

As a significant parameter for quantitatively comparing SERS performance, the enhancement factor (EF) of the nanoporous Ag-decorated $\text{Ag}_7\text{O}_8\text{NO}_3$ micro-pyramids was determined by computing the ratio of SERS to normal Raman scattering (NRS) of R6G (Figure S10) using the following expression:

$$EF = \frac{I_{SERS} N_{Ref}}{I_{Ref} N_{SERS}} = \frac{I_{SERS} C_{Ref} V_{Ref} S_{SERS}}{I_{Ref} C_{SERS} V_{SERS} S_{Ref}} \quad (2)$$

where I_{SERS} and I_{NRS} correspond to the SERS and NRS intensities, respectively. For estimation of EF, a $10 \mu\text{L } 10^{-11} \text{ M}$ and two $10 \mu\text{L}$ R6G ethanol solutions with concentration of 10^{-11} M and 10^{-2} M were dropped on the substrates ($2 \times 2 \text{ mm}^2$) and polyvinyl chloride film ($\pi \times 1^2 \text{ mm}^2$), respectively. The EF for the band at 1648 cm^{-1} was calculated to be 5.6×10^8 (detailed calculation process can be found in the first part of the Supplemental Material), revealing the high SERS activity of the fabricated SERS substrate.

In addition to SERS sensitivity, uniformity of Raman signals is another crucial indicator for SERS substrates. As shown in Figure 3c, SERS spectra were collected from 10 random points on the fabricated SERS substrate. It can be found that the characteristic spectral peaks' intensities of R6G at 1648 cm^{-1} collected from 10 random points on the fabricated SERS substrate are very similar, and the RSD value was calculated to be 10.72% (Figure 3d). The point-to-point RSD of substrates that are eligible for quantitative analysis is typically thought to need to be less than 20% [73]. Thus, the nanoporous Ag-decorated $\text{Ag}_7\text{O}_8\text{NO}_3$ micro-pyramids have also shown outstanding uniformity for SERS measurements besides high sensitivity.

In order to ulteriorly demonstrate the practical applicability of the SERS substrate, crystal violet (CV) was chosen as another probe molecules. CV, an alkaline dye, is an excellent dye. It is widely used when dyeing leather, paper, and other materials. Additionally, reagent goods, pharmaceutical intermediates, and industry all make extensive use of CV. As dosage is increased, a substantial amount of CV is emitted into wastewater, causing visible color changes in water bodies in terms of chromaticity. It seriously harms people, animals, and plants, and this harm could be long-lasting and dangerous due to its carcinogenicity, mutagenicity, and reproductive toxicity [74,75]. Before it may be discharged, waste water that contains CV must be treated to meet regulations. Therefore, it is essential to monitor the concentration of them. The characteristic peaks of CV are clearly observed and can be attributed to phenyl ring breathing mode (914 cm^{-1}), C-phenyl, C-H in-plane antisymmetric stretching (1176 cm^{-1}), C-phenyl in-plane antisymmetric stretching (1585 cm^{-1} and 1618 cm^{-1}) [76,77]. Additionally, the linear fitting result show that the R^2 value are 0.99 (Figure 4b) for CV. The LOD were calculated down to $9.6 \times 10^{-13} \text{ M}$. It could be observed that Raman signals of CV collected from different points on the nanoporous Ag-decorated $\text{Ag}_7\text{O}_8\text{NO}_3$ micro-pyramids are consistent (Figure S11a), and the RSD values are evaluated to be 10.55% (CV, 1618 cm^{-1}) (Figure S11b). Those results indicate that the fabricated substrate has high SERS sensitivity and superior uniformity again.

The applicability of the SERS substrate was also tested towards the detection of pesticide (thiram). As a low toxicity fungicide, thiram is widely used in the elimination of agricultural pests. The relatively strong Raman peaks of thiram were assigned to S-S stretching mode (560 cm^{-1}), CN stretching mode and the symmetric CH_3 deformation mode (1384 cm^{-1}), and CN stretching vibrations and CH_3 rocking mode (1517 cm^{-1}) [7,78]. The linear fitting result shows that the R^2 value is 0.99 (Figure 4d). The LOD was calculated down to $1.3 \times 10^{-15} \text{ M}$ ($3.12 \times 10^{-10} \text{ ppm}$), which is below the maximal residue limit (MRL) of 7 ppm in fruit prescribed by the U.S. Environmental Protection Agency (EPA) [79–81]. Additionally, it was showed that relatively consistent Raman intensities were found in all SERS active points (Figure S11c). Through statistical calculation, the RSD of the Raman intensity at 1384 cm^{-1} was $\sim 13.93\%$ (Figure S11d). Such experimental results indicate that the nanoporous Ag-decorated $\text{Ag}_7\text{O}_8\text{NO}_3$ micro-pyramids can serve as effective SERS substrates for sensitive detection of pesticide molecules.

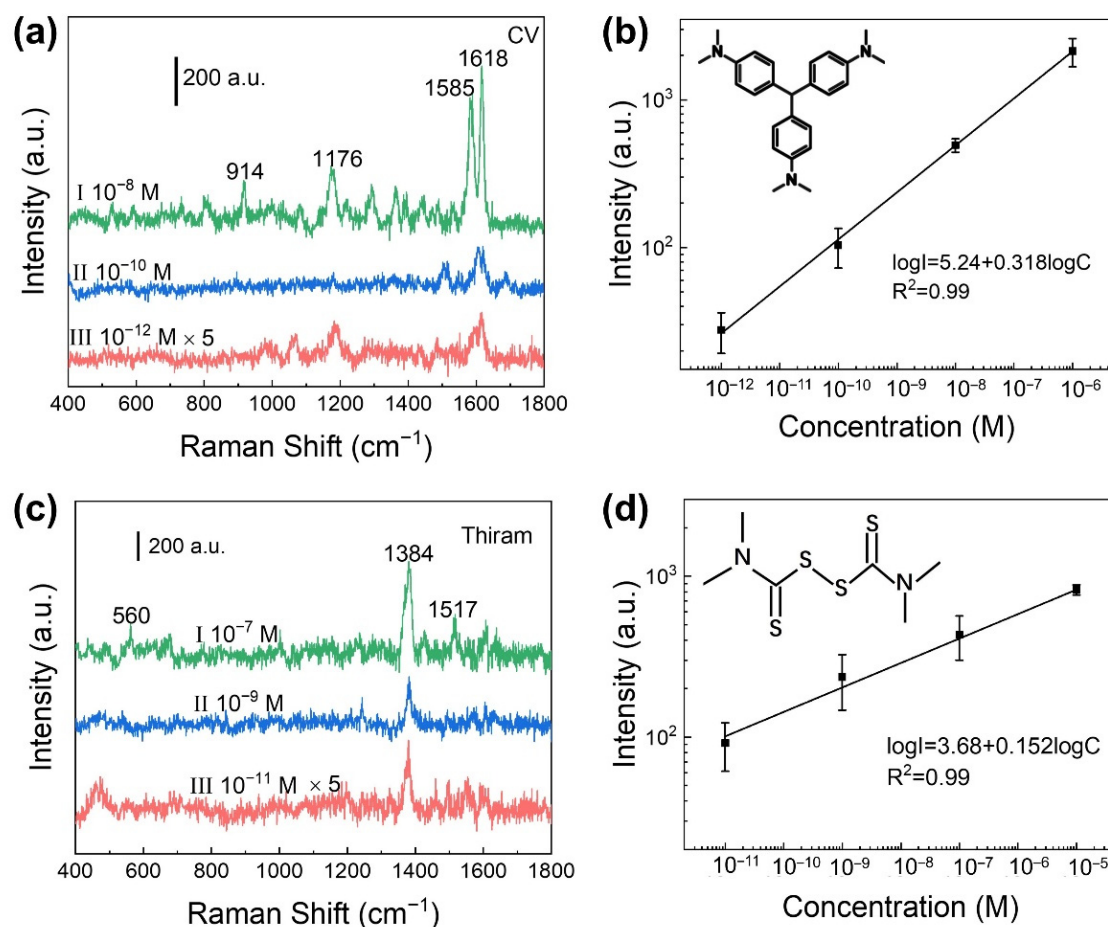


Figure 4. (a) SERS spectra of (Curve I) 10^{-8} , (Curve II) 10^{-10} and (Curve III) 10^{-12} M CV collected from nanoporous Ag-decorated $\text{Ag}_7\text{O}_8\text{NO}_3$ micro-pyramids. (b) Linear relationship between the logarithmic intensities (1618 cm^{-1} peak) and the concentrations of CV. (c) SERS spectra of (Curve I) 10^{-7} , (Curve II) 10^{-9} and (Curve III) 10^{-11} M thiram from nanoporous Ag-decorated $\text{Ag}_7\text{O}_8\text{NO}_3$ micro-pyramids. (d) Linear relationship between the logarithmic intensities (1384 cm^{-1} peak) and the concentrations of thiram.

4. Conclusions

A facile method is presented to prepare nanoporous Ag nanoparticles-decorated $\text{Ag}_7\text{O}_8\text{NO}_3$ micro-pyramids through the chemical reduction of the as-electrodeposited $\text{Ag}_7\text{O}_8\text{NO}_3$ micro-pyramids using NaBH_4 . By regulating the concentration of NaBH_4 , the nanoporous Ag-decorated $\text{Ag}_7\text{O}_8\text{NO}_3$ micro-pyramids with highly accessible surfaces were obtained, and a larger number of Ag nanopores were formed on the surfaces of the $\text{Ag}_7\text{O}_8\text{NO}_3$ pyramids. The nanoporous with an average diameter of 40 nm can serve as analyte containers, which efficiently trap and enrich analytes, and also provide high density SERS hotspots giving rise to outstanding SERS performance. For the analyte molecules such as rhodamine 6G, crystal violet and thiram, the fabricated nanoporous Ag-decorated $\text{Ag}_7\text{O}_8\text{NO}_3$ micro-pyramids substrates can realize sensitive and uniform detection. The fabricated nanoporous Ag-decorated $\text{Ag}_7\text{O}_8\text{NO}_3$ micro-pyramids have potential applications in the rapid, sensitive, and direct detection of dyes and pesticides, and the method may also be extended to fabrication of other nanoporous materials. Consequently, the easy and time-saving fabrication process and the outstanding SERS performance ensure the nanoporous Ag-decorated $\text{Ag}_7\text{O}_8\text{NO}_3$ micro-pyramids have promising applications in trace detection of harmful pollutants.

Supplementary Materials: The following supporting information can be downloaded at: <https://www.mdpi.com/article/10.3390/chemosensors10120539/s1>, 1. Estimation of enhancement factor. Figure S1: The fabricated nanoporous Ag-decorated $\text{Ag}_7\text{O}_8\text{NO}_3$ micro-pyramids on ITO glass (2 cm \times 0.5 cm) (left) and the actual substrate cut down for SERS detection (0.5 cm \times 0.5 cm) (right). Figure S2: The X-ray diffraction pattern of the electrodeposited materials. Figure S3: Energy-dispersive X-ray (EDX) mapping images of electrodeposited materials. Figure S4: SEM images of the $\text{Ag}_7\text{O}_8\text{NO}_3$ micro-pyramids' morphology evolution under the different electrodeposition voltage. Figure S5: SEM images of the $\text{Ag}_7\text{O}_8\text{NO}_3$ micro-pyramids' morphology evolution under different electrodeposition time. Figure S6: Energy-dispersive X-ray (EDX) mapping images of nanoporous Ag-decorated $\text{Ag}_7\text{O}_8\text{NO}_3$ micro-pyramids. Figure S7: SERS signals of R6G (10^{-6} M) collected from nanoporous Ag-decorated $\text{Ag}_7\text{O}_8\text{NO}_3$ micro-pyramids reduced by using NaBH_4 solution with different concentrations. Figure S8: Morphology of nanoporous Ag-decorated $\text{Ag}_7\text{O}_8\text{NO}_3$ micro-pyramids reduced using 5 mM NaBH_4 solution. Figure S9: SERS signals of R6G (10^{-7} M) collected from $\text{Ag}_7\text{O}_8\text{NO}_3$ micro-pyramids and $\text{Ag}_7\text{O}_8\text{NO}_3$ micro-pyramids by chemical reduction. Figure S10: SERS spectrum of 10^{-11} M R6G absorbed on the nanoporous Ag-decorated $\text{Ag}_7\text{O}_8\text{NO}_3$ micro-pyramids, and the normal Raman spectrum of R6G polyvinyl chloride film. Figure S11: Raman spectra of CV (10^{-5} M) and thiram (10^{-5} M), and the RSD values of 1618 cm^{-1} (CV) and 1384 cm^{-1} (thiram) peaks, respectively. Table S1: Comparison of LODs between various SERS substrates

Author Contributions: Conceptualization, L.G. and C.Z.; methodology, L.G. and C.Z.; validation, L.G. and C.Z.; formal analysis, L.G. and C.Z.; investigation, L.G.; resources, C.Z., Y.Y. and H.T.; data curation, L.G.; writing—original draft preparation, L.G.; writing—review and editing, C.Z., X.W. and H.T.; supervision, C.Z.; project administration, C.Z.; funding acquisition, C.Z. and H.T. All authors have read and agreed to the published version of the manuscript.

Funding: This research was funded by the National Natural Science Foundation of China (No 22175002 and 51972308) and Natural Science Foundation of Anhui Province (No 1808085J12, 2008085ME171 and 201903a07020021) for the experiments and characterizations.

Institutional Review Board Statement: Not applicable.

Informed Consent Statement: Not applicable.

Data Availability Statement: Not applicable.

Acknowledgments: The authors are grateful to Haichao Zhai of the University of Chemistry and Chemical Engineering, Anhui University, Hefei, China, for much helpful discussion of the manuscript.

Conflicts of Interest: The authors declare no conflict of interest.

References

1. Liu, Y.; Zhou, H.; Hu, Z.; Yu, G.; Yang, D.; Zhao, J. Label and Label-Free Based Surface-Enhanced Raman Scattering for Pathogen Bacteria Detection: A Review. *Biosens. Bioelectron.* **2017**, *94*, 131–140. [[CrossRef](#)]
2. Langer, J.; Jimenez de Aberasturi, D.; Aizpurua, J.; Alvarez-Puebla, R.A.; Auguie, B.; Baumberg, J.J.; Bazan, G.C.; Bell, S.E.J.; Boisen, A.; Brolo, A.G.; et al. Present and Future of Surface-Enhanced Raman Scattering. *ACS Nano* **2020**, *14*, 28–117. [[CrossRef](#)]
3. Vendrell, M.; Maiti, K.K.; Dhaliwal, K.; Chang, Y.-T. Surface-Enhanced Raman Scattering in Cancer Detection and Imaging. *Trends Biotechnol.* **2013**, *31*, 249–257. [[CrossRef](#)]
4. Pérez-Jiménez, A.I.; Lyu, D.; Lu, Z.; Liu, G.; Ren, B. Surface-Enhanced Raman Spectroscopy: Benefits, Trade-Offs and Future Developments. *Chem. Sci.* **2020**, *11*, 4563–4577. [[CrossRef](#)]
5. Xu, K.; Zhou, R.; Takei, K.; Hong, M. Toward Flexible Surface-Enhanced Raman Scattering (SERS) Sensors for Point-of-Care Diagnostics. *Adv. Sci.* **2019**, *6*, 1900925. [[CrossRef](#)]
6. Ultrasensitive Surface-Enhanced Raman Scattering Detection in Common Fluids. Available online: <https://www.pnas.org/doi/10.1073/pnas.1518980113> (accessed on 1 August 2022).
7. Kumar, S.; Goel, P.; Singh, J.P. Flexible and Robust SERS Active Substrates for Conformal Rapid Detection of Pesticide Residues from Fruits. *Sens. Actuators B Chem.* **2017**, *241*, 577–583. [[CrossRef](#)]
8. Kumar, S.; Gahlaut, S.K.; Singh, J.P. Sculptured Thin Films: Overcoming the Limitations of Surface-Enhanced Raman Scattering Substrates. *Appl. Surf. Sci. Adv.* **2022**, *12*, 100322. [[CrossRef](#)]
9. Shen, Y.; Zhou, J.; Liu, T.; Tao, Y.; Jiang, R.; Liu, M.; Xiao, G.; Zhu, J.; Zhou, Z.-K.; Wang, X.; et al. Plasmonic Gold Mushroom Arrays with Refractive Index Sensing Figures of Merit Approaching the Theoretical Limit. *Nat. Commun.* **2013**, *4*, 2381. [[CrossRef](#)]
10. Gellé, A.; Jin, T.; de la Garza, L.; Price, G.D.; Besteiro, L.V.; Moores, A. Applications of Plasmon-Enhanced Nanocatalysis to Organic Transformations. *Chem. Rev.* **2020**, *120*, 986–1041. [[CrossRef](#)]

11. Loiseau, A.; Asila, V.; Boitel-Aullen, G.; Lam, M.; Salmain, M.; Boujday, S. Silver-Based Plasmonic Nanoparticles for and Their Use in Biosensing. *Biosensors* **2019**, *9*, 78. [[CrossRef](#)]
12. Li, Z.; Kurouski, D. Plasmon-Driven Chemistry on Mono- and Bimetallic Nanostructures. *Acc. Chem. Res.* **2021**, *54*, 2477–2487. [[CrossRef](#)]
13. Zhang, Q.; Lee, Y.H.; Phang, I.Y.; Lee, C.K.; Ling, X.Y. Hierarchical 3D SERS Substrates Fabricated by Integrating Photolithographic Microstructures and Self-Assembly of Silver Nanoparticles. *Small* **2014**, *10*, 2703–2711. [[CrossRef](#)]
14. Liu, D.; Wang, X.; He, D.; Dao, T.D.; Nagao, T.; Weng, Q.; Tang, D.; Wang, X.; Tian, W.; Golberg, D.; et al. Magnetically Assembled Ni@Ag Urchin-Like Ensembles with Ultra-Sharp Tips and Numerous Gaps for SERS Applications. *Small* **2014**, *10*, 2564–2569. [[CrossRef](#)]
15. Pazos-Pérez, N.; Barbosa, S.; Rodríguez-Lorenzo, L.; Aldeanueva-Potel, P.; Pérez-Juste, J.; Pastoriza-Santos, I.; Alvarez-Puebla, R.A.; Liz-Marzán, L.M. Growth of Sharp Tips on Gold Nanowires Leads to Increased Surface-Enhanced Raman Scattering Activity. *J. Phys. Chem. Lett.* **2010**, *1*, 24–27. [[CrossRef](#)]
16. Iarossi, M.; Hubarevich, A.; Iachetta, G.; Dipalo, M.; Huang, J.-A.; Darvill, D.; De Angelis, F. Probing ND7/23 Neuronal Cells before and after Differentiation with SERS Using Sharp-Tipped Au Nanopyramid Arrays. *Sens. Actuators B Chem.* **2022**, *361*, 131724. [[CrossRef](#)]
17. Marshall, A.R.L.; Stokes, J.; Viscomi, F.N.; Proctor, J.E.; Gierschner, J.; Bouillard, J.-S.G.; Adawi, A.M. Determining Molecular Orientation via Single Molecule SERS in a Plasmonic Nano-Gap. *Nanoscale* **2017**, *9*, 17415–17421. [[CrossRef](#)]
18. Park, W.-H.; Park, S.-G.; Kang, M.; Hyun, M.S.; Choi, N.; Kim, D.-H.; Choo, J. Direct Visualization of a Surface-Enhanced Raman Spectroscopy Nano-Gap via Electrostatic Force Microscopy: Dependence on Charge Transfer from the Underlying Surface Nano-Gap Distance. *Appl. Surf. Sci.* **2019**, *479*, 874–878. [[CrossRef](#)]
19. Minati, L.; Maniglio, D.; Benetti, F.; Chiappini, A.; Speranza, G. Multimodal Gold Nanostars as SERS Tags for Optically-Driven Doxorubicin Release Study in Cancer Cells. *Materials* **2021**, *14*, 7272. [[CrossRef](#)]
20. Jalani, G.; Cerruti, M. Nano Graphene Oxide-Wrapped Gold Nanostars as Ultrasensitive and Stable SERS Nanoprobes. *Nanoscale* **2015**, *7*, 9990–9997. [[CrossRef](#)]
21. Qingquan, G.; Xinfu, M.; Yu, X.; Wei, T.; Hui, Z. Green Synthesis and Formation Mechanism of Ag Nanoflowers Using L-Cysteine and the Assessment of Ag Nanoflowers as SERS Substrates. *Colloids Surf. Physicochem. Eng. Asp.* **2017**, *530*, 33–37. [[CrossRef](#)]
22. He, H.; Sun, D.-W.; Pu, H.; Huang, L. Bridging Fe₃O₄@Au Nanoflowers and Au@Ag Nanospheres with Aptamer for Ultrasensitive SERS Detection of Aflatoxin B1. *Food Chem.* **2020**, *324*, 126832. [[CrossRef](#)]
23. Jung, G.-B.; Kim, J.-H.; Burm, J.S.; Park, H.-K. Fabrication of Chitosan-Silver Nanoparticle Hybrid 3D Porous Structure as a SERS Substrate for Biomedical Applications. *Appl. Surf. Sci.* **2013**, *273*, 179–183. [[CrossRef](#)]
24. Liu, K.; Bai, Y.; Zhang, L.; Yang, Z.; Fan, Q.; Zheng, H.; Yin, Y.; Gao, C. Porous Au–Ag Nanospheres with High-Density and Highly Accessible Hotspots for SERS Analysis. *Nano Lett.* **2016**, *16*, 3675–3681. [[CrossRef](#)]
25. Hu, J.; Jiang, R.; Zhang, H.; Guo, Y.; Wang, J.; Wang, J. Colloidal Porous Gold Nanoparticles. *Nanoscale* **2018**, *10*, 18473–18481. [[CrossRef](#)]
26. Zheng, P.; Wu, L.; Raj, P.; Mizutani, T.; Szabo, M.; Hanson, W.A.; Barman, I. A Dual-Modal Single-Antibody Plasmonic Spectro-Immunoassay for Detection of Small Molecules. *Small* **2022**, *18*, 2200090. [[CrossRef](#)]
27. Zheng, P.; Kasani, S.; Wu, N. Converting Plasmonic Light Scattering to Confined Light Absorption and Creating Plexcitons by Coupling a Gold Nano-Pyramid Array onto a Silica-Gold Film. *Nanoscale Horiz.* **2019**, *4*, 516–525. [[CrossRef](#)]
28. Zheng, P.; Raj, P.; Wu, L.; Szabo, M.; Hanson, W.A.; Mizutani, T.; Barman, I. Leveraging Nanomechanical Perturbations in Raman Spectro-Immunoassays to Design a Versatile Serum Biomarker Detection Platform. *Small* **2022**, *18*, 2204541. [[CrossRef](#)]
29. Khan, M.N.; Zharnikov, M. Irradiation Promoted Exchange Reaction with Disulfide Substituents. *J. Phys. Chem. C* **2013**, *117*, 14534–14543. [[CrossRef](#)]
30. Wang, J.; Liu, X.; Li, R.; Li, Z.; Wang, X.; Wang, H.; Wu, Y.; Jiang, S.; Lu, Z. Formation Mechanism and Characterization of Immiscible Nanoporous Binary Cu-Ag Alloys with Excellent Surface-Enhanced Raman Scattering Performance by Chemical Dealloying of Glassy Precursors. *Inorg. Chem. Front.* **2020**, *7*, 1127–1139. [[CrossRef](#)]
31. Fu, H.-Y.; Lang, X.-Y.; Hou, C.; Wen, Z.; Zhu, Y.-F.; Zhao, M.; Li, J.-C.; Zheng, W.-T.; Liu, Y.-B.; Jiang, Q. Nanoporous Au/SnO/Ag Heterogeneous Films for Ultrahigh and Uniform Surface-Enhanced Raman Scattering. *J. Mater. Chem. C* **2014**, *2*, 7216–7222. [[CrossRef](#)]
32. Feng, L.; Zhou, Y.; Wang, W. Hollow and Nanoporous Ag Sub-Microcubes as SERS Substrates. *Chem. Commun.* **2022**. [[CrossRef](#)]
33. Koya, A.N.; Zhu, X.; Ohannesian, N.; Yanik, A.A.; Alabastri, A.; Proietti Zaccaria, R.; Krahe, R.; Shih, W.-C.; Garoli, D. Nanoporous Metals: From Plasmonic Properties to Applications in Enhanced Spectroscopy and Photocatalysis. *ACS Nano* **2021**, *15*, 6038–6060. [[CrossRef](#)]
34. Zhang, L.; Chen, L.; Liu, H.; Hou, Y.; Hirata, A.; Fujita, T.; Chen, M. Effect of Residual Silver on Surface-Enhanced Raman Scattering of Dealloyed Nanoporous Gold. *J. Phys. Chem. C* **2011**, *115*, 19583–19587. [[CrossRef](#)]
35. Bekana, D.; Liu, R.; Li, S.; Liu, J.-F. Fabrication of Nanoporous Silver Film by Dealloying Ag/ α -Fe₂O₃ Nanocomposite for Surface-Enhanced Raman Spectroscopy. *Sens. Actuators B Chem.* **2019**, *286*, 94–100. [[CrossRef](#)]
36. Li, R.; Liu, X.J.; Wang, H.; Wu, Y.; Chu, X.M.; Lu, Z.P. Nanoporous Silver with Tunable Pore Characteristics and Superior Surface Enhanced Raman Scattering. *Corros. Sci.* **2014**, *84*, 159–164. [[CrossRef](#)]

37. Wang, C.; Zhu, S.; Liang, Y.; Cui, Z.; Wu, S.; Qin, C.; Luo, S.; Inoue, A. Understanding the Macroscopical Flexibility/Fragility of Nanoporous Ag: Depending on Network Connectivity and Micro-Defects. *J. Mater. Sci. Technol.* **2020**, *53*, 91–101. [[CrossRef](#)]
38. Lu, L.; Eychmüller, A. Ordered Macroporous Bimetallic Nanostructures: Design, Characterization, and Applications. *Acc. Chem. Res.* **2008**, *41*, 244–253. [[CrossRef](#)]
39. Qin, Y.; Mo, F.; Yao, S.; Wu, Y.; He, Y.; Yao, W. Facile Synthesis of Porous Ag Crystals as SERS Sensor for Detection of Five Methamphetamine Analogs. *Molecules* **2022**, *27*, 3939. [[CrossRef](#)]
40. Khinevich, N.; Bandarenka, H.; Zavatski, S.; Girel, K.; Tamulevičienė, A.; Tamulevičius, T.; Tamulevičius, S. Porous Silicon—A Versatile Platform for Mass-Production of Ultrasensitive SERS-Active Substrates. *Microporous Mesoporous Mater.* **2021**, *323*, 111204. [[CrossRef](#)]
41. Sanguansap, Y.; Karn-orachai, K.; Laocharoensuk, R. Tailor-Made Porous Striped Gold-Silver Nanowires for Surface Enhanced Raman Scattering Based Trace Detection of β -Hydroxybutyric Acid. *Appl. Surf. Sci.* **2020**, *500*, 144049. [[CrossRef](#)]
42. Clay, M.; Cui, Q.; Sha, Y.; Chen, J.; Rondinone, A.J.; Wu, Z.; Chen, J.; Gu, Z. Galvanic Synthesis of Bi-Modal Porous Metal Nanostructures Using Aluminum Nanoparticle Templates. *Mater. Lett.* **2012**, *88*, 143–147. [[CrossRef](#)]
43. Kang, S.; Shin, W.; Kang, K.; Choi, M.-H.; Kim, Y.-J.; Kim, Y.-K.; Min, D.-H.; Jang, H. Revisiting of Pd Nanoparticles in Cancer Treatment: All-Round Excellence of Porous Pd Nanoplates in Gene-Thermo Combinational Therapy. *ACS Appl. Mater. Interfaces* **2018**, *10*, 13819–13828. [[CrossRef](#)]
44. Petri, M.V.; Ando, R.A.; Camargo, P.H.C. Tailoring the Structure, Composition, Optical Properties and Catalytic Activity of Ag–Au Nanoparticles by the Galvanic Replacement Reaction. *Chem. Phys. Lett.* **2012**, *531*, 188–192. [[CrossRef](#)]
45. An, Y.; Tian, Y.; Wei, C.; Tao, Y.; Xi, B.; Xiong, S.; Feng, J.; Qian, Y. Dealloying: An Effective Method for Scalable Fabrication of 0D, 1D, 2D, 3D Materials and Its Application in Energy Storage. *Nano Today* **2021**, *37*, 101094. [[CrossRef](#)]
46. Rurainsky, C.; Manjón, A.G.; Hiege, F.; Chen, Y.-T.; Scheu, C.; Tschulik, K. Electrochemical Dealloying as a Tool to Tune the Porosity, Composition and Catalytic Activity of Nanomaterials. *J. Mater. Chem. A* **2020**, *8*, 19405–19413. [[CrossRef](#)]
47. Ngô, B.-N.D.; Roschning, B.; Albe, K.; Weissmüller, J.; Markmann, J. On the Origin of the Anomalous Compliance of Dealloying-Derived Nanoporous Gold. *Scr. Mater.* **2017**, *130*, 74–77. [[CrossRef](#)]
48. Wang, Y.; Zhao, L.; Zhao, Y.; Wang, W.Y.; Liu, Y.; Gu, C.; Li, J.; Zhang, G.; Huang, T.J.; Yang, S. Electrocarving during Electrodeposition Growth. *Adv. Mater.* **2018**, *30*, 1805686. [[CrossRef](#)]
49. Breyfogle, B.E.; Phillips, R.J.; Switzer, J.A. Epitaxial Electrodeposition of Silver Oxide Nitrate ($\text{Ag}(\text{Ag}_3\text{O}_4)_2\text{NO}_3$) onto Highly-Oriented Conducting Metal Oxides in the Lead-Thallium-Oxygen System. *Chem. Mater.* **1992**, *4*, 1356–1360. [[CrossRef](#)]
50. Tanaka, R.; Takata, S.; Katayama, M.; Takahashi, R.; Grepstad, J.K.; Tybell, T.; Matsumoto, Y. Photocatalytic Synthesis of Silver-Oxide Clathrate $\text{Ag}_7\text{O}_8\text{NO}_3$. *J. Electrochem.* **2010**, *157*, E181. [[CrossRef](#)]
51. Waterhouse, G.I.N.; Metson, J.B.; Bowmaker, G.A. Synthesis, Vibrational Spectra and Thermal Stability of Ag_3O_4 and Related $\text{Ag}_7\text{O}_8\text{X}$ Salts. *Polyhedron* **2007**, *26*, 3310–3322. [[CrossRef](#)]
52. Grier, D.; Ben-Jacob, E.; Clarke, R.; Sander, L.M. Morphology and Microstructure in Electrochemical Deposition of Zinc. *Phys. Rev. Lett.* **1986**, *56*, 1264–1267. [[CrossRef](#)]
53. Chung, A.J.; Huh, Y.S.; Erickson, D. Large Area Flexible SERS Active Substrates Using Engineered Nanostructures. *Nanoscale* **2011**, *3*, 2903. [[CrossRef](#)]
54. Wagner, M.; Andrew Lin, K.-Y.; Oh, W.-D.; Lisak, G. Metal-Organic Frameworks for Pesticidal Persistent Organic Pollutants Detection and Adsorption—A Mini Review. *J. Hazard. Mater.* **2021**, *413*, 125325. [[CrossRef](#)]
55. Chen, Q.; Zhao, L.; Liu, H.; Ding, Q.; Jia, C.; Liao, S.; Cheng, N.; Yue, M.; Yang, S. Nanoporous Silver Nanorods as Surface-Enhanced Raman Scattering Substrates. *Biosens. Bioelectron.* **2022**, *202*, 114004. [[CrossRef](#)]
56. Yuan, Y.; Zhou, Z.; Luo, J.; Dan, Z.; Qin, F.; Chang, H. (1 1 1)-Facet Dominant Ultrafine Nanoporous Silver as SERS Substrates with High Sensitivities and Ultrahigh Detection Limits. *Appl. Surf. Sci.* **2021**, *556*, 149820. [[CrossRef](#)]
57. Lang, X.Y.; Guan, P.F.; Zhang, L.; Fujita, T.; Chen, M.W. Characteristic Length and Temperature Dependence of Surface Enhanced Raman Scattering of Nanoporous Gold. *J. Phys. Chem. C* **2009**, *113*, 10956–10961. [[CrossRef](#)]
58. Wi, J.-S.; Kim, J.D.; Lee, W.; Choi, H.; Kwak, M.; Song, J.; Lee, T.G.; Ok, J.G. Inkjet-Printable Nanoporous Ag Disk Arrays Enabling Coffee-Ring Effect-Driven Analyte Enrichment Towards Practical SERS Applications. *Int. J. Precis. Eng. Manuf.-Green Technol.* **2022**, *9*, 421–429. [[CrossRef](#)]
59. Hildebrandt, P.; Stockburger, M. Surface-Enhanced Resonance Raman Spectroscopy of Rhodamine 6G Adsorbed on Colloidal Silver. *J. Phys. Chem.* **1984**, *88*, 5935–5944. [[CrossRef](#)]
60. Li, Z.; Jiang, S.; Huo, Y.; Ning, T.; Liu, A.; Zhang, C.; He, Y.; Wang, M.; Li, C.; Man, B. 3D Silver Nanoparticles with Multilayer Graphene Oxide as a Spacer for Surface Enhanced Raman Spectroscopy Analysis. *Nanoscale* **2018**, *10*, 5897–5905. [[CrossRef](#)]
61. Hussain, A.; Sun, D.-W.; Pu, H. Bimetallic Core Shelled Nanoparticles ($\text{Au}@\text{AgNPs}$) for Rapid Detection of Thiram and Dicyandiamide Contaminants in Liquid Milk Using SERS. *Food Chem.* **2020**, *317*, 126429. [[CrossRef](#)]
62. Zhu, C.; Meng, G.; Zheng, P.; Huang, Q.; Li, Z.; Hu, X.; Wang, X.; Huang, Z.; Li, F.; Wu, N. A Hierarchically Ordered Array of Silver-Nanorod Bundles for Surface-Enhanced Raman Scattering Detection of Phenolic Pollutants. *Adv. Mater.* **2016**, *28*, 4871–4876. [[CrossRef](#)]
63. Long, G.L.; Winefordner, J.D. Limit of Detection. A Closer Look at the IUPAC Definition. *Anal. Chem.* **1983**, *55*, 712A–724A. [[CrossRef](#)]

64. Zhou, Y.; Marar, A.; Kner, P.; Ramasamy, R.P. Charge-Directed Immobilization of Bacteriophage on Nanostructured Electrode for Whole-Cell Electrochemical Biosensors. *Anal. Chem.* **2017**, *89*, 5734–5741. [[CrossRef](#)]
65. Li, A.; Xin, X.; Zhang, T.; Xu, T.; Li, L.; Liu, C.; Li, W.; Li, J.; Li, Y.; Lu, R. Facile Synthesis of Two-Dimensional PA-Ag@C Film for Highly Sensitive SERS Detection. *Surf. Interface Anal.* **2023**, *55*, 71–81. [[CrossRef](#)]
66. Wen, P.; Yang, F.; Ge, C.; Li, S.; Xu, Y.; Chen, L. Self-Assembled Nano-Ag/Au@Au Film Composite SERS Substrates Show High Uniformity and High Enhancement Factor for Creatinine Detection. *Nanotechnology* **2021**, *32*, 395502. [[CrossRef](#)]
67. Kong, L.; Chen, J.; Huang, M. GO/Au@Ag Nanobones Decorated Membrane for Simultaneous Enrichment and on-Site SERS Detection of Colorants in Beverages. *Sens. Actuators B Chem.* **2021**, *344*, 130163. [[CrossRef](#)]
68. Sun, Q.; Xu, Y.; Gao, Z.; Zhou, H.; Zhang, Q.; Xu, R.; Zhang, C.; Yao, H.; Liu, M. High-Performance Surface-Enhanced Raman Scattering Substrates Based on the ZnO/Ag Core-Satellite Nanostructures. *Nanomaterials* **2022**, *12*, 1286. [[CrossRef](#)]
69. Qu, L.-L.; Geng, Z.-Q.; Wang, W.; Yang, K.-C.; Wang, W.-P.; Han, C.-Q.; Yang, G.-H.; Vajtai, R.; Li, D.-W.; Ajayan, P.M. Recyclable Three-Dimensional Ag Nanorod Arrays Decorated with O-g-C₃N₄ for Highly Sensitive SERS Sensing of Organic Pollutants. *J. Hazard. Mater.* **2019**, *379*, 120823. [[CrossRef](#)]
70. Xu, D.; Duan, L.; Jia, W.; Yang, G.; Gu, Y. Fabrication of Ag@Fe₂O₃ Hybrid Materials as Ultrasensitive SERS Substrates for the Detection of Organic Dyes and Bilirubin in Human Blood. *Microchem. J.* **2021**, *161*, 105799. [[CrossRef](#)]
71. Zhang, W.; Cai, Y.; Qian, R.; Zhao, B.; Zhu, P. Synthesis of Ball-Like Ag Nanorod Aggregates for Surface-Enhanced Raman Scattering and Catalytic Reduction. *Nanomaterials* **2016**, *6*, 99. [[CrossRef](#)]
72. Cheng, M.; Li, C.; Li, W.; Liu, Y. Trace Cd²⁺ Ions Detection on the Flower-Like Ag@CuO Substrate. *Nanomaterials* **2020**, *10*, 1664. [[CrossRef](#)]
73. Pu, H.; Huang, Z.; Xu, F.; Sun, D.-W. Two-Dimensional Self-Assembled Au-Ag Core-Shell Nanorods Nanoarray for Sensitive Detection of Thiram in Apple Using Surface-Enhanced Raman Spectroscopy. *Food Chem.* **2021**, *343*, 128548. [[CrossRef](#)]
74. Liu, B.; Jiang, W.; Wang, H.; Yang, X.; Zhang, S.; Yuan, Y.; Wu, T.; Du, Y. A Surface Enhanced Raman Scattering (SERS) Microdroplet Detector for Trace Levels of Crystal Violet. *Microchim. Acta* **2013**, *180*, 997–1004. [[CrossRef](#)]
75. Li, B.; Shi, Y.; Cui, J.; Liu, Z.; Zhang, X.; Zhan, J. Au-Coated ZnO Nanorods on Stainless Steel Fiber for Self-Cleaning Solid Phase Microextraction-Surface Enhanced Raman Spectroscopy. *Anal. Chim. Acta* **2016**, *923*, 66–73. [[CrossRef](#)]
76. Meng, W.; Hu, F.; Zhang, L.-Y.; Jiang, X.-H.; Lu, L.-D.; Wang, X. SERS and DFT Study of Crystal Violet. *J. Mol. Struct.* **2013**, *1035*, 326–331. [[CrossRef](#)]
77. Harraz, F.A.; Ismail, A.A.; Bouzid, H.; Al-Sayari, S.A.; Al-Hajry, A.; Al-Assiri, M.S. Surface-Enhanced Raman Scattering (SERS)-Active Substrates from Silver Plated-Porous Silicon for Detection of Crystal Violet. *Appl. Surf. Sci.* **2015**, *331*, 241–247. [[CrossRef](#)]
78. Zheng, X.; Chen, Y.; Chen, Y.; Bi, N.; Qi, H.; Qin, M.; Song, D.; Zhang, H.; Tian, Y. High Performance Au/Ag Core/Shell Bipyramids for Determination of Thiram Based on Surface-Enhanced Raman Scattering: High Performance Au/Ag Core/Shell Bipyramids for Determination of Thiram Based on SERS. *J. Raman Spectrosc.* **2012**, *43*, 1374–1380. [[CrossRef](#)]
79. Sun, L.; Wang, C. Highly Sensitive and Rapid Surface Enhanced Raman Spectroscopic (SERS) Determination of Thiram on the Epidermis of Fruits and Vegetables Using A Silver Nanoparticle-Modified Fibrous Swab. *Anal. Lett.* **2020**, *53*, 973–983. [[CrossRef](#)]
80. Sun, H.; Liu, H.; Wu, Y. A Green, Reusable SERS Film with High Sensitivity for in-Situ Detection of Thiram in Apple Juice. *Appl. Surf. Sci.* **2017**, *416*, 704–709. [[CrossRef](#)]
81. Chen, M.; Luo, W.; Liu, Q.; Hao, N.; Zhu, Y.; Liu, M.; Wang, L.; Yang, H.; Chen, X. Simultaneous In Situ Extraction and Fabrication of Surface-Enhanced Raman Scattering Substrate for Reliable Detection of Thiram Residue. *Anal. Chem.* **2018**, *90*, 13647–13654. [[CrossRef](#)]